A&A, 711, A225 (2026)
https://doi.org/10.1051/0004-6361/202453643

Astronomy & Astrophysics

Modeling accretion columns in accretion-powered pulsars

II. Directly observable column emission

S. Falkner[1,⋆], E. Sokolova-Lapa[1,⋆], F.-W. Schwarm[1], M. Bissinger[1], R. Ballhausen[2,3], K. A. Postnov[4], T. Dauser[1], P. B. Hemphill[5], K. Pottschmidt[2,6,†], F. Fürst[7], P. Kretschmar[7], G. Schönherr[1,8], M. T. Wolff[9], P. A. Becker[10], M. Falanga[11,12††], C. Ferrigno[13,14], R. E. Rothschild[15], R. Staubert[16], I. Kreykenbohm[1], and J. Wilms[1]

[1] Dr. Karl Remeis-Observatory & ECAP, University of Erlangen-Nuremberg, Sternwartstr. 7, 96049 Bamberg, Germany
[2] NASA Goddard Space Flight Center, Astrophysics Science Division, Greenbelt, MD 20771, USA
[3] CRESST, Department of Astronomy, University of Maryland, College Park, MD 20742, USA
[4] Sternberg Astronomical Institute, M. V. Lomonosov Moscow State University, Universitetskij pr., 13, Moscow 119992, Russia
[5] Boston Fusion Corp., 70 Westview, Suite 100, Lexington, MA 02421, USA
[6] CRESST and Center for Space Science and Technology, UMBC, Baltimore, MD 21250, USA
[7] European Space Astronomy Center (ESA/ESAC), Science Operations Department, Villanueva de la Cañada, 28691 Madrid, Spain
[8] Leibniz-Institut für Astrophysik Potsdam (AIP), An der Sternwarte 16, 14482 Potsdam, Germany
[9] Space Science Division, Naval Research Laboratory, Washington, DC 20375-5352, USA
[10] Department of Physics & Astronomy, George Mason University, Fairfax, VA 22030-4444, USA
[11] International Space Science Institute, Hallerstrasse 6, 3012 Bern, Switzerland
[12] Physikalisches Institut, University of Bern, Sidlerstrasse 5, 3012 Bern, Switzerland
[13] ISDC, Department of Astronomy, University of Geneva, Chemin d'Ecogia 16, 1290 Versoix, Switzerland
[14] INAF, Osservatorio Astronomico di Brera, Via E. Bianchi 46, I-23807 Merate, Italy
[15] Astronomy and Astrophysics Dept., University of California San Diego, La Jolla, CA 92075, USA
[16] Institut für Astronomie und Astrophysik, Universität Tübingen, Sand 1, 72076 Tübingen, Germany

Received 31 January 2024 / Accepted 9 April 2026

ABSTRACT

Context. Modeling the observed emission from highly magnetized accreting neutron stars is essential for interpreting their X-ray spectra and variability. This task is challenging due to the dynamic, multidimensional nature of the accretion columns and the strong gravitational field. Radiation propagation outside the column, within the neutron star's gravitational field, significantly shapes the observed emission and its variability with rotational phase. Geometry – the location of the magnetic poles and the observer's inclination – is one of the key factors influencing the observables due to the anisotropy of the problem.

Aims. In this work, we study how visibility effects in the gravitational field of the neutron star influence the direct emission from an accretion column, highlighting their importance when interpreting plasma parameters from observed spectra.

Methods. Building on the physical model from the previous paper in this series, we investigate the directly observable X-ray flux from one and two columns with fan-beam wall emission, down-boosted by the bulk flow, focusing on the impact of geometry.

Results. We find that the observed flux strongly depends on the geometrical setup, which we illustrate across various observables. Particularly notable are special geometries in which a column on the far side of the neutron star aligns with the line of sight. In these cases, shadowing and strong light bending produce a narrow intense peak in pulse profiles at soft energies and a pronounced dip at higher energies ($\gtrsim$20 keV). The combination of shadowing and height dependence of emission also leads to spectral softening. Flux-derived luminosities can be overestimated by up to a factor of 10. The fundamental cyclotron resonant scattering feature (CRSF) appears predominantly in emission across geometries, and we discuss possible causes.

Conclusions. Our results demonstrate that geometry has a major impact on pulse profiles, phase-averaged spectra, phase–energy maps, and the anisotropy factor relevant for luminosity estimates. Future studies should include the reflected component in addition to the direct emission considered here, and account for a more accurate treatment of resonant redistribution in the CRSF-forming region.

Key words. radiative transfer – relativistic processes – methods: numerical – stars: neutron – X-rays: binaries

1. Introduction

In this work, we study the predicted observed emission from a strongly magnetized neutron star ($B \sim 10^{12}$ G), accreting at high mass-accretion rates ($\dot{M} \gtrsim 10^{17}\,\mathrm{g\,s^{-1}}$), sufficient to form a radiation-dominated shock inside the accretion column. In our previous work in this series (Falkner et al. 2026, hereafter Paper I), we combined physical emission models for the continuum and cyclotron resonant scattering feature (CRSF) formation to investigate height- and angle-dependent spectra in the rest frame of the neutron star, taking into account the influence of the fast-moving bulk flow at the outer wall of the accretion column. There, we also introduced our light-bending code to obtain the relativistic projection of emission regions in the Schwarzschild metric onto the sky of a remote observer. In this paper, we study in detail how gravitational effects and geometry – a set of angles defining the locations of the magnetic poles and the observer's inclination – influence the observational signatures across the

⋆ Corresponding authors: sebastian.falkner@fau.de; ekaterina.sokolova-lapa@fau.de
† Deceased 17 June 2025.
†† Deceased 6 March 2025.

energy- and phase-resolved flux. While the geometric dependence of pulse profiles is generally well established, its effect on spectra and spectral features has been far less explored, due to the lack of models that combine all necessary dimensions.

The observed emission encodes information about the plasma state under the extreme conditions. The key question, however, is how the radiation field – representative of the local plasma conditions in the accretion column – is modified for a distant observer by visibility effects due to the viewing angle, shape, and location of the emission regions and the neutron star's rotation. Due to the complexity of the problem, theoretical studies often compare the spectral behavior of the flux in the neutron star rest frame directly with observational data, assuming isotropic emission and a distance to the source (e.g., West et al. 2017; Wolff et al. 2016; Sokolova-Lapa et al. 2021). Alternatively, some works qualitatively compare the appearance of specific spectral features between the two frames, implicitly assuming that rotation, geometric, and light-bending effects do not significantly affect their observability (e.g., Mushtukov et al. 2021; Loudas et al. 2024). Meanwhile, codes developed to account for light bending and neutron star geometry are commonly used in a combination with purely phenomenological emission profiles, which do not contain spectral information (e.g., Markozov & Mushtukov 2024; Ferrigno et al. 2011; Laycock et al. 2025). To reliably assess how the physical parameters inferred from observations may deviate from their true values, these different aspects of the problem need to be treated within a unified framework. At the high mass-accretion rates studied here, the interplay between height-dependent emission and gravitational effects makes the inference of plasma parameters particularly nontrivial.

Combining energy- and angle-dependent modeled emission is challenging because of the large parameter space that arises when exploring observables for different neutron star geometries. The only extensive earlier effort to link spectral formation, including cyclotron resonances, with the two-dimensional hydrodynamic structure of the accretion column and the relativistic projection of a vertically extended emission region with height-dependent radiation fields was carried out in a series of works by Rebetzky et al. (1988, 1989), Kraus et al. (1989), and Nollert et al. (1989). In cases in which the accretion column was directed away from the observer, they found a relativistic pulse-profile signature in the form of a strong peak, consistent with earlier findings by, for example, Meszaros & Riffert (1988). By incorporating spectral information, Nollert et al. (1989) further showed that this feature is energy-dependent, disappearing above ~25 keV. The role of geometry, however, was not addressed in this series of works.

Similar to models that adopted phenomenological fan-beam profiles for the accretion column and accounted for the Lorentz transformation of these profiles from the fast-moving plasma to the neutron star rest frame (e.g., Kraus et al. 2003; Mushtukov et al. 2018; Markozov & Mushtukov 2024), Kraus et al. (1989) and Nollert et al. (1989) showed that a significant fraction of the radiation, varying with photon energy, is intercepted by the neutron star surface. This arises from the same mechanism as is discussed in Paper I: energy-dependent boosting of the radiation field by the fast-moving flow in the outer layer of the accretion channel. In all of the works mentioned above, this intercepted radiation is assumed to be isotropically re-emitted ("reflected") by the neutron star atmosphere, thereby adding a halo-like component to the pulse profile.

Here, we extend the study of an accretion column emission model similar to that of Nollert et al. (1989), focusing on the effects of neutron star geometry and going beyond pulse profile modeling. Adopting a column model with fixed physical conditions, we investigate how various observables change with geometry and how physical parameters derived from observations may differ from their true values. We also illustrate how the appearance of spectral features can be altered. Compared to previous works of this type, our model for the column emission in the neutron star rest frame additionally includes the effects of higher cyclotron harmonics (see Paper I). In this work, we focus only on the directly observable emission from the accretion column. We emphasize that it is crucial to understand the signatures originating from the column at different geometries before they are modified by contributions from the reflected component.

This paper is organized as follows. In Sect. 2 we discuss the consequences of height-dependent emission and downward boosting in the column model, together with the main geometrical visibility constraints in curved space-time. Section 3 presents an extensive study of various observables, including pulse profiles, phase-averaged spectra, and phase-energy maps, for different neutron star geometries. Section 4 discusses the results and their implication. Finally, we summarize and conclude this study in Sect. 5.

2. Role of geometry and light bending

In Paper I, we presented a framework that combined several modeling components to obtain the emission from accretion column. The accretion column radius, $r_{\rm AC} = 647$ m, height, $h_{\rm AC} = 5$ km, and the height-dependent velocity, $\upsilon(h)$, and temperature, $T(h)$, are set by the Postnov et al. (2015) model, which provide the continuum emission in the regime of saturated Comptonization, $\mathcal{I}_E$ (Paper I, Eq. 1). This emission is then processed in the optically thin outermost layer of the column wall, where the plasma velocity remains close to the free-fall value, υ_0, using the convolution model of Schwarm et al. (2017b,a) for cyclotron scattering. This combination yields a height-, angle-, and energy-dependent emission profile $I(E', \mu', h)'$, where $\mu' = \cos\eta'$ denotes the angle between the magnetic field and the photon emission direction (Paper I, Fig. 2). The specific intensity in the rest frame of the neutron star, $I^{\star}{}_{E^{\star}}(\mu^{\star})$, is obtained by applying the Lorentz transformation to $I'{}_{E'}(\mu')$. The ray-tracing code described in Paper I is then applied to compute the observed flux, $F_E(\phi; i, \Theta_{\rm AC}, \Phi_{\rm AC})$, at each rotational phase, ϕ. The flux depends strongly on the observer inclination, i, relative to the rotational axis and the location of the accretion column(s) given by the polar angle, $\Theta_{\rm AC}$, and azimuthal angle, $\Phi_{\rm AC}$ (Paper I, Fig. 4). For a complete summary of parameters and model details, see Table 1 and Sect. 2 of Paper I.

In this section, we examine how general relativistic effects constrain the directly observable flux (Sect. 2.1) and produce distinct visibility regions for emission close to the neutron star (Sect. 2.2). Throughout this work, simulations are performed for a neutron star with mass $M_{\rm NS} = 1.4\,{\rm M}_{\odot}$ and radius $R_{\rm NS} = 10$ km. However, we illustrate the influence of compactness on visibility in Sect. 2.2 and discuss its impact on observables in Sect. 4.

2.1. Observable emission and luminosity

There are general geometrical constraints on the observable emission of the accretion column due to the presence of the neutron star. Only a fraction of the emission from the column is directly observable. In particular, this means that photons exceeding a certain emission angle (dependent on the height) will hit the neutron star. For a conical accretion column the

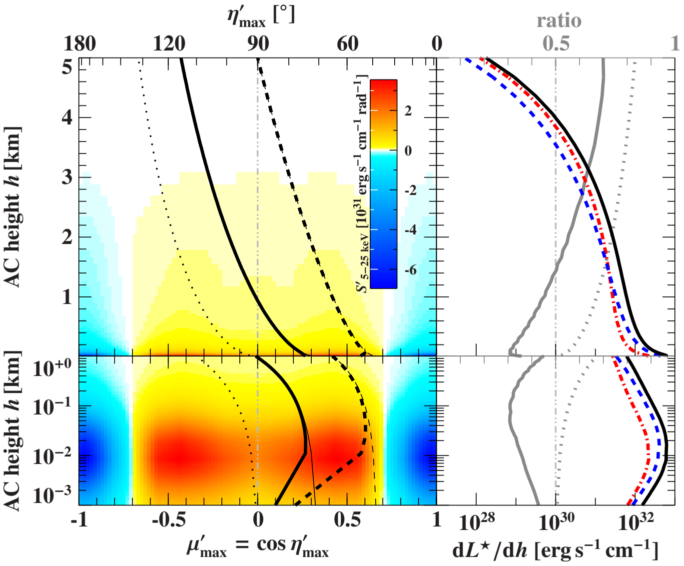

Fig. 1. Left: Maximum observable emission angle, $\eta'_{\max}$. Photons emitted with larger angles hit the neutron star. The dotted line accounts for light bending, and the solid and dashed lines for bulk velocities, υ_0 and $2\upsilon_0$, respectively. The dash-dot-dotted vertical line indicates the case in a flat space-time. The color map indicates the line strength, S', of the CRSF in the energy range from 5 keV to 25 keV. Right: Total flux emitted from the column shown as a solid black line, flux directed to the neutron star as a dashed blue line, and escaping flux as a dash-dotted red line. The ratio of escaping to total flux is shown as a solid gray line, while the dotted gray one shows the ratio assuming isotropic emission in the rest frame of the neutron star. Bottom: Zoom-in on the bottom part of the column shown at the top panel in linear scale; now the flux and ratios are displayed on a logarithmic scale.

maximum directly observable emission angle in the rest frame of the neutron star is given by

$$\eta^{\star}{}_{\max}(h) = \pi - \arcsin\left(\frac{R_{\rm NS}}{R_{\rm NS}+h}\sqrt{\frac{1-\frac{R_{\rm s}}{R_{\rm NS}+h}}{1-\frac{R_{\rm s}}{R_{\rm NS}}}}\right), \tag{1}$$

depending on the height, h, in the column (Paper I, Eq. A.12 and Eq. A.7). Here $R_{\rm s}$ denotes the Schwarzschild radius of the neutron star with mass $M_{\rm NS}$ and radius $R_{\rm NS}$. Equation (1) is also suitable for cylindrical columns with small radii. Figure 1 visualizes the maximum observable emission angle, $\eta'_{\max}$, in the rest frame of the emitting plasma for different bulk velocities[1]. Generally $\eta'_{\max}$ decreases with decreasing height, independent of the boosting factor. The boosting, however, clearly decreases the range of observable emission angles dramatically. As a result, in our case 58% of the intrinsic luminosity $L^{\star}$ (Paper I, Eq. 11) emitted from the column hits the neutron star, while it would be only 31% without accounting for relativistic boosting. The fraction of the flux not intercepted by the neutron star increases from 31% at the bottom of the column to 70% at a height of 5 km, which is also significantly lower than in the case without relativistic boosting.

The actual X-ray luminosity, L (hereafter referred to as "luminosity"), in the band from 1 keV to 100 keV is given by

$$L = D^2 \int_{1\,\rm keV}^{100\,\rm keV} \int_0^{2\pi} \int_{-1}^{1} F_E \mathrm{d}\cos i \,\mathrm{d}\phi \,\mathrm{d}E, \tag{2}$$

[1] Note that the bulk velocity is constant over most of the column and only decreases at the bottom part (Paper I, Fig. 5).

where F_E is the observed flux (Paper I, Eq. A.22) and D is the distance of the observer to the source. It represents the observed luminosity accounting for a potential anisotropy of the flux. To relate this quantity to the intrinsic luminosity, $L^{\star}$ (Paper I, Eq. 11), we have to account for gravitational effects (Thorne 1977). Additionally L in Eq. (2) corresponds only to the directly observed luminosity,

$$L \approx \left(1 - \frac{R_{\rm s}}{R_{\rm NS}}\right) L^{\star}\Big|_{\eta^{\star}<\eta^{\star}{}_{\max}} = (1+z_{\rm NS})^{-2}\, L^{\star}\Big|_{\eta^{\star}<\eta^{\star}{}_{\max}}\,. \tag{3}$$

For our model, $L = 0.8{\times}10^{37}\,\mathrm{erg\,s^{-1}}$ for one column, which is only 35% of the corresponding total intrinsic luminosity, $L^{\star}$. Note that in general L cannot be deduced from observations since information is missing on how the emission depends on the inclination, i. The best approximation is to assume F_E to be constant in i, in order to get the flux-derived "isotropic" luminosity,

$$L_{4\pi} = 2D^2 \int_{1\,\rm keV}^{100\,\rm keV} \int_0^{2\pi} F_E \mathrm{d}\phi \,\mathrm{d}E. \tag{4}$$

2.2. Shadowing and strong light bending

Depending on their visibility, we can divide the vicinity of the neutron star into three regions as shown in Fig. 2. First, there is the normal region which covers mostly the area in front of the neutron star and includes only the photon trajectories with one possibility to reach the observer. Second is the small shadow region on the far side of the neutron star, directly above the surface hidden from view. This shadow region transitions into the third region, the region of strong light bending in which each point possesses two possible trajectories reaching the observer (see Paper I). This region is a result of the strongly curved space-time in the vicinity of the neutron star. The transition of the emitting region, i.e., the accretion column, between those regions over the neutron star's rotational phase causes significant changes in the observables. In the following we quantitatively describe the boundary of these regions.

Based on the analytical approximation for the photon trajectory (Paper I, Eq. A.14), the height of the shadow above the neutron star's surface can be written as

$$h_{\rm S}(\Psi) = \frac{2\left(\frac{b_{\rm NS}}{R_{\rm s}}\right)^2 R_{\rm s}}{C_\Psi^2 + \sqrt{C_\Psi^4 - 4C_\Psi(C_\Psi-2)\left(\frac{b_{\rm NS}}{R_{\rm s}}\right)^2}} - R_{\rm NS}, \tag{5}$$

with

$$C_\Psi = \begin{cases} 1-\cos(\Psi_{\rm p}) & 0^\circ \le \Psi < \Psi_{\rm p} \\ 1-\cos(2\Psi_{\rm p}-\Psi) \quad \text{for} & \Psi_{\rm p} \le \Psi \le 180^\circ \\ C_{2\pi-\Psi} & 180^\circ < \Psi < 360^\circ \end{cases},$$

where $b_{\rm NS} = R_{\rm NS}/\sqrt{1-R_{\rm s}/R_{\rm NS}}$ is the impact parameter of the neutron star (Paper I, Eq. A.7), and $\Psi_{\rm p} = \arccos(1-1/(1-R_{\rm s}/R_{\rm NS}))$ is the polar angle of the point of emission with respect to the observer at the periastron of the corresponding photon trajectory (Paper I, Fig. A.1). The maximum shadow height is reached for $\Psi = 180^\circ$ directly on the opposite side of the neutron star along the line of sight; that is, $h_{\rm S}^{\max} = h_{\rm S}(180^\circ)$. For our model, featuring a neutron star with a compactness $R_{\rm s}/R_{\rm NS} = 0.43$ we get $h_{\rm S}^{\max} = 1291$ m. Figure 2 also shows how the maximum shadow height increases for decreasing compactness of the neutron star. For example, for a neutron star with a

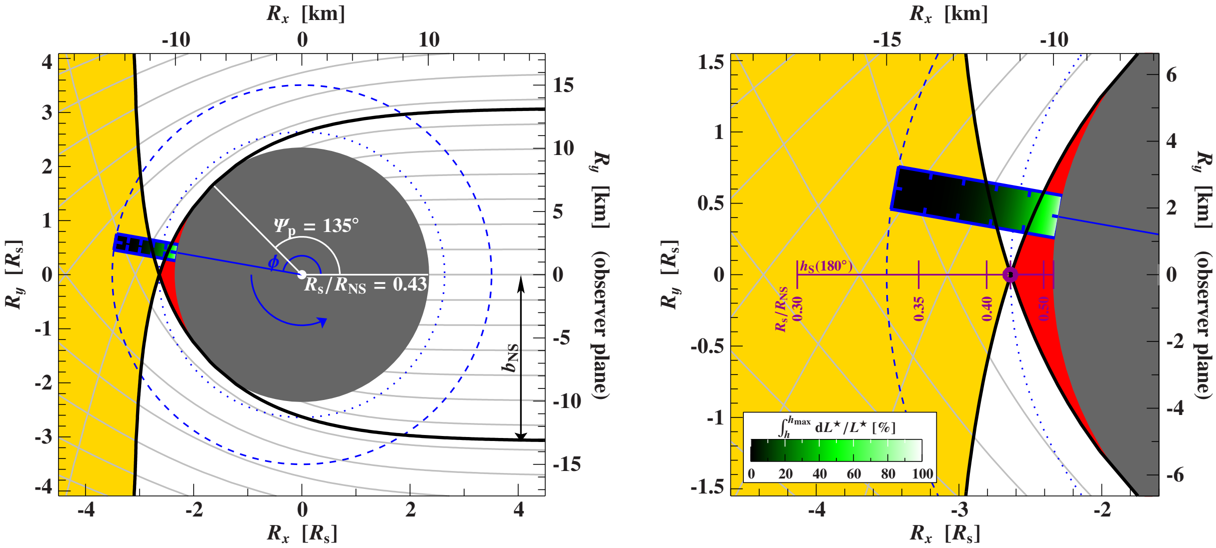

Fig. 2. Regions of visibility around a neutron star. Left: Principal regions divided by the boundary trajectory (solid black line). The boundary trajectory touches the neutron star (gray) in the periastron denoted by the polar angle, Ψ_p. The gray lines represent a grid of possible trajectories to the observer at infinity to the right. For points in the red, white, and yellow region there are no, one, or two possible trajectories reaching the observer, respectively. The blue rectangle indicates the accretion column (r_{AC} = 647 m, h_{max} = 5 km) where its cumulative intrinsic luminosity, $\int_h^{h_{max}} dL^\star/L^\star$, is color coded (see right panel). The tic marks are separated by 1 km. The dashed and dotted blue lines show the path of the accretion column around the neutron star at height h_{max} and $h_S(180°)$, respectively. The geometry is chosen such that the column rotates around the z axis in the x–y plane, i.e., $i = \Theta_{AC} = 90°$. Right: Zoom-in on the shadow region. The purple circle marks the maximum height of the shadow above the neutron star's surface, $h_S(180°) = 1291$ m. The evolution of this shadow height for neutron stars of a different compactness is indicated by the purple markers.

compactness of 0.3 (i.e., 14 km, 1.4 $M_\odot$) the maximum shadow height is already at 8 km above the surface. Increasing the compactness to 0.67 causes the shadow to vanish completely, i.e., $h_S(R_s/R_{NS} \geq 0.67) \equiv 0$.

Using Eq. (A.19) in Paper I we could relate Ψ to the observer's inclination, i, the polar angle of the column, Θ_{AC}, and the rotational phase, ϕ. For geometries with $i + \Theta_{AC1/2} = 180°$ and phase $\phi = 180° - \Phi_{AC1/2}$, the line of sight is aligned with one of the B field axes, i.e., the column is centered around $\Psi = 180°$. In such cases the column is projected as a perfect Einstein ring (Einstein 1936, see also Fig. 5), assuming that the height of the column exceeds approximately the maximum shadow height. A ring projection is possible as long as the shadow point is within the column,

$$180° - \Delta\Psi_{ring} < i + \Theta_{AC} < 180° + \Delta\Psi_{ring}, \tag{6}$$

where

$$\Delta\Psi_{ring} \approx \arctan\left(\frac{r_{AC}}{R_{NS} + h_S^{max}}\right). \tag{7}$$

Further, the column is only passing through or within the shadow region if

$$\Psi_p + \Delta\Psi_{AC} < i + \Theta_{AC} < 360° - \Psi_p - \Delta\Psi_{AC}, \tag{8}$$

where Ψ_p relates to the periastron and $\Delta\Psi_{AC} = \arctan(r_{AC}/R_{NS})$ is the half opening angle of accretion column at its base. For our setup (Paper I, Table 1) we get $\Delta\Psi_{ring} = 3.3°$, $\Psi_p = 135°$ and $\Delta\Psi_{AC} = 4.7°$. The small value of $\Delta\Psi_{ring}$ translates into a very narrow phase range in which the Einstein ring is visible. Furthermore, as $\Delta\Psi_{AC}$ is also small, there are only few geometries for which this effect can even occur.

3. Geometry-dependent observables

The constraints on emission from different column regions imply that not only observables sensitive to the instantaneous angle between the line of sight and the magnetic axis, such as pulse profiles, but also angle-averaged properties, like phase-averaged spectra and total luminosity, will vary depending on the geometry. Here, we show and compare the results of the simulations for energy- and phase-resolved observed flux, $F_E(\phi)$, for a single column and two-column configurations. In the latter case, the columns are identical and typically assumed to be antipodal. We find that asymmetric configurations have only a small impact on the results presented in the following section, aside from introducing expected asymmetry and increased complexity to the pulse profile shapes. A detailed investigation of asymmetric setups is beyond the scope of this paper. However, we present selected results for a chosen asymmetric case (see, also, Appendix A).

3.1. Energy-integrated pulse profiles

Figure 3 shows the shapes of the observed pulse profiles for various antipodal two-column configurations seen under different angles. We integrated the flux over the 1–100 keV range and normalized it as follows:

$$\tilde{F} = \frac{F - \langle F \rangle_\phi}{\sigma_F}, \tag{9}$$

where $\langle F \rangle_\phi$ the phase-averaged flux, and σ_F is the standard deviation. This normalization emphasizes the shape of the pulse profile and makes the pulse shapes comparable. We note that the shape of the integrated pulse profiles is largely determined by soft X-ray energies, $\lesssim$10 keV.

The pulse profiles in Fig. 3 exhibit a range of shapes, from single-peaked sinusoidal to broad plateaus and double-peaked

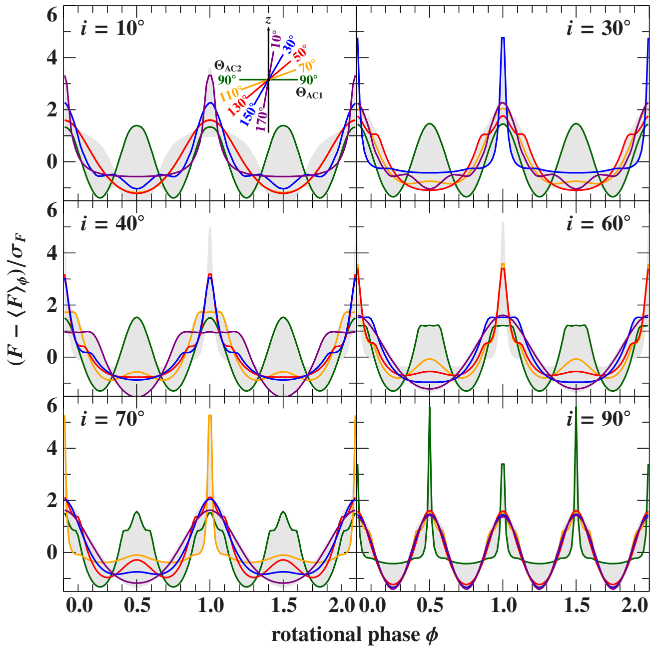

Fig. 3. Energy-integrated normalized pulse profiles for different antipodal two-column geometries. Each panel shows a different observer inclination, i, for different B field inclinations $\Theta_{\mathrm{AC}1/2}$ indicated with different colors in the upper left panel. The gray band represents the contour, in which the pulse profiles vary at the shown observer inclination.

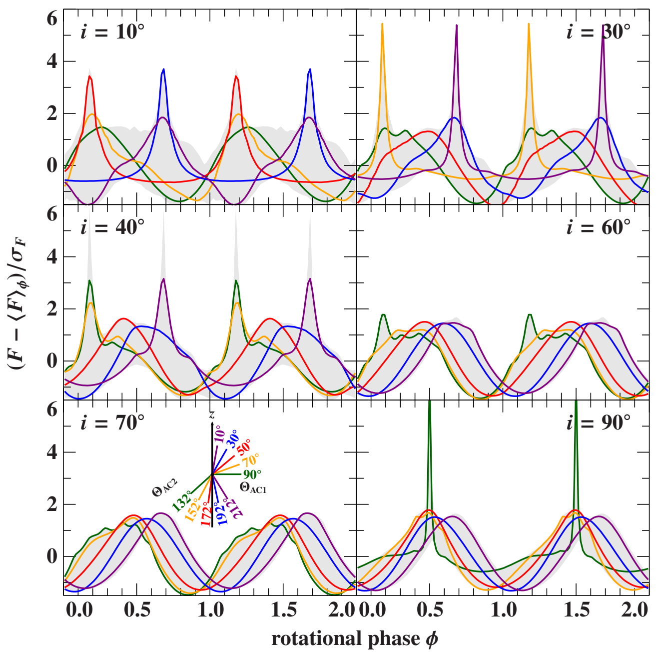

Fig. 4. Energy-integrated normalized pulse profiles. Same as in Fig. 3, but for the asymmetric two-column setup, with $\Delta\Phi_{\mathrm{AC}} = \Phi_{\mathrm{AC}1} - \Phi_{\mathrm{AC}2} - \pi = -65^\circ$.

sinusoidal. In the antipodal setup, all profiles are axisymmetric around $\phi = 0$ and 0.5. Pulse profiles for asymmetric configurations are shown in Fig. 4. The general behavior is similar to the profiles in the antipodal case. Due to the axis-symmetric geometry of the columns and their emission pattern, each column's contribution to the pulse profile remains axis-symmetric, regardless of the columns' polar angle, Θ_{AC}. The asymmetry of the pulse profile arises from the phase displacement $\Delta\Phi_{\mathrm{AC}} \neq 0^\circ$.

We note the narrow but prominent peaks in the pulse profiles shown in Figs. 3 and 4, which arise from strong light bending (see Sect. 2.2). Figure 5 shows the relativistic projection of a neutron star with two antipodal accretion columns onto the observer's sky (Paper I, Fig. A.1) in comparison with the flat-space-time projection at different phases. In the latter case, the second accretion column is only visible for $\phi = 0.4$, whereas in the relativistic case it appears prominent and more luminous than the front column in all phases. At $\phi = 0$, the back column forms an Einstein ring, allowing the observer to see its full circumference and producing the narrow peaks in the pulse profiles, as described previously for relativistic accretion columns and polar caps (see, e.g., Pechenick et al. 1983; Meszaros & Riffert 1988). Here we emphasize the shift of these peaks for an asymmetric setup and its implication for constraining the geometry based on such features.

3.2. Pulsed fraction

A simple measure for the variability of the observed flux with the rotational phase is the pulsed fraction, which we define here as (see Ferrigno et al. 2023, for other commonly used definitions of this quantity)

$$\delta F = \frac{\max(F) - \min(F)}{\max(F) + \min(F)}. \tag{10}$$

This parameter encodes information about the underlying geometry, as shown in Fig. 6. In the single-column case, the pulsed fraction reaches its maximum value of 1 for two types of geometries. For $i + \Theta_{\mathrm{AC}1} \approx 180^\circ$ with $\Theta_{\mathrm{AC}1} > 90^\circ$, a high pulsed fraction arises from the prominent narrow peaks caused by strong light bending (Fig. 3). For geometries with $i \approx \Theta_{\mathrm{AC}1}$ and $\Theta_{\mathrm{AC}1} < 90^\circ$, the accretion column is seen directly from above at certain phases. In our model, since the top of the column does not emit, this line of sight produces a deep dip in the pulse profile, which also increases the pulsed fraction.

Figure 6 (right) shows the pulsed fraction for the two-column antipodal configuration. In this case, the column located on the far side of the neutron star always appears brighter than the one in front. The pulsed fraction is therefore dominated by peaks from the opposite-side column for geometries where $i + \Theta_{\mathrm{AC}1,2} \approx 180^\circ$.

3.3. Luminosity

Figure 7 shows the anisotropy factor of the flux-derived isotropic luminosity, $L_{4\pi}/L$ (see Sect. 2.1), and its dependency on the geometry. If only one accretion column is present, the anisotropy factor varies over several orders of magnitude. Looking directly into the column from above ($i = 0^\circ$, $\Theta_{\mathrm{AC}1} = 0^\circ$) the luminosity is underestimated by a factor of 10^3, while it is overestimated by a factor of 22 when the column is constantly on the opposite side ($i = 0^\circ$, $\Theta_{\mathrm{AC}1} = 180^\circ$). Figure 7 also shows that the enhancement in luminosity occurs for geometries where $i + \Theta_{\mathrm{AC}1,2} \approx 180^\circ$. The enhancement in the flux-derived luminosity is due to the high visibility caused by strong light bending (Fig. 2), while the column is projected twice or even as ring (Fig. 5). For two antipodal columns, however, the anisotropy factor ranges only from 0.8 to 11 as the second column compensates the extreme amplitudes present when only one column is considered. Nevertheless, even in the case of two columns there is a significant systematic error for the flux-derived luminosity. It is impossible to determine this systematic error without knowing the physical parameters of the system.

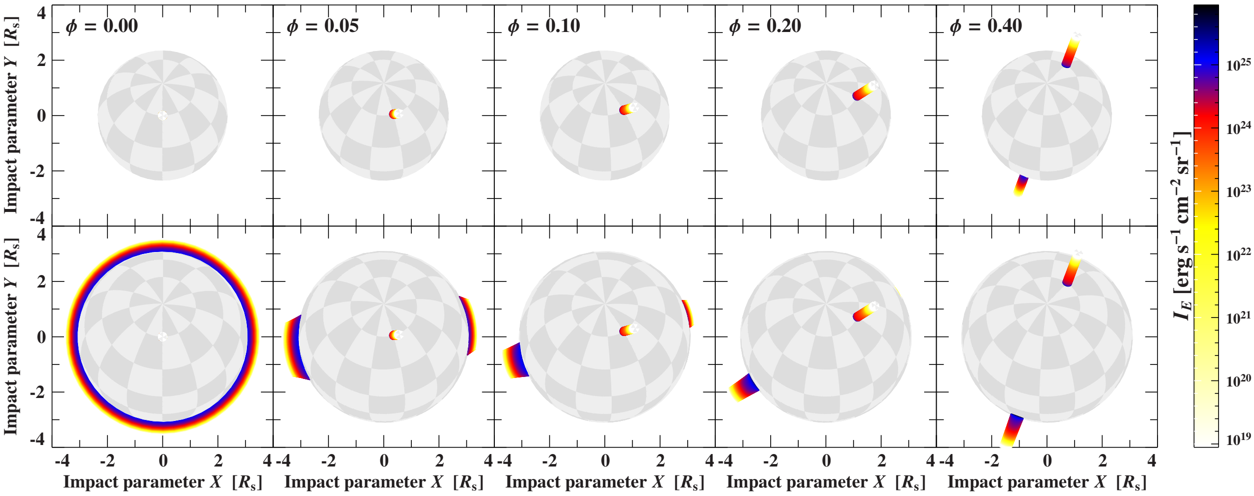

Fig. 5. Sky projection without (top) and with light bending (bottom). The projection is parameterized with the impact point (X, Y) (Paper I, Eq. A.15) in units of the Schwarzschild radius, R_s, at different rotational phases, ϕ. The system is seen under $i = 30°$ and consists of two antipodal accretion columns, with $\Theta_{AC1} = 30°$ and $\Theta_{AC2} = 150°$, and $\Phi_{AC1} = 0$ and $\Phi_{AC2} = 180°$. The color represents the specific intensity I_E in the rest frame of the observer.

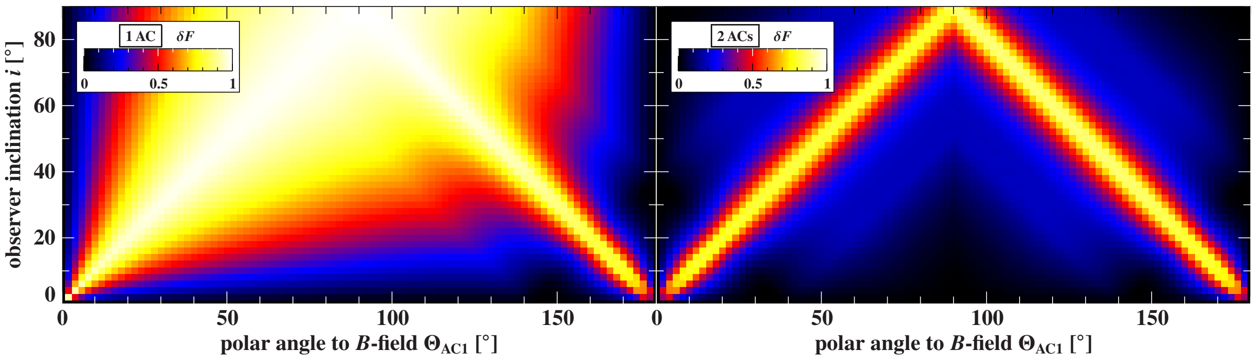

Fig. 6. Pulsed fraction of energy-integrated pulse profiles for different geometries. Left: Case of one accretion column. Right: Case of two antipodal accretion columns.

The strong Doppler boosting in the column significantly increases the anisotropy of the originally fan-beam emission. In our model, the boosting shifts the maximum of the emitted flux to larger angles, and therefore most of column's emission is directed downward (Paper I, Fig. 5). In combination with the fact that the observable emission angle, $\eta^\star$, increases with the polar angle, Ψ (Fig. 2), very large flux-derived luminosities become possible. For our model, Eq. (1) gives maximum observable emission angles $\eta^\star{}_{max}(1\,\mathrm{km}) = 110°$ and $\eta^\star{}_{max}(5\,\mathrm{km}) = 132°$, while the intrinsic column luminosity, $\mathrm{d}L^\star/\mathrm{d}\mu^\star$, peaks at $\eta^\star = 131°$. Thus, the directions of peak emissivity align with the angles most enhanced by light bending.

3.4. Spectra

We extend our analysis to emission resolved in energy, with primary focus on phase-averaged spectra across different geometries, while also discussing the impact on phase-resolved flux. Figures 8 and 9 show the spectral dependence of the phase-averaged flux in the observer frame, $\langle F_E \rangle_\phi$, for a few selected combinations of i and Θ_{AC1}, for the single- and two-column cases, respectively. Both the continuum and cyclotron lines strongly depend on the geometry. To study the behavior of the spectral characteristics across parameter space quantitatively, we sample the spectra over the full range of i and Θ_{AC1}, and fit them with phenomenological models as described in the following section. We generally find that the results for the chosen asymmetric configurations are very similar to the antipodal case.

3.4.1. Continuum

To describe the behavior of the observed continuum, we used a power-law with a high energy exponential cutoff,

$$\texttt{CutoffPL}(E) \propto E^{-\Gamma} \exp(-E/E_{\mathrm{fold}})\,, \tag{11}$$

where Γ is the photon index and E_{fold} is the folding energy. We fit Eq. (11) to both the height- and angle-integrated continuum in the rest frame of the neutron star, $\mathrm{d}L^\star/\mathrm{d}E^\star$, and the phase-averaged observed continua for different geometries, $\langle F_E \rangle_\phi\,(i, \Theta_{AC})$, in the energy range 1–100 keV. Quantities derived from the phase-averaged flux are denoted with an overline. For example, $\overline{\Gamma} = \Gamma(\langle F_E \rangle_\phi)$ refers to the photon index obtained by fitting a `CutoffPL` model to the phase-averaged spectrum $\langle F_E \rangle_\phi$.

The energy dependence of the specific intensity in the rest frame of the plasma, $\mathcal{I}'_{E'}$ (Paper I, Eq. 1), corresponds to a `CutoffPL` spectrum with $\Gamma' = 0$ and $E'_{\mathrm{fold}} = kT$; that is, the characteristic plasma temperature at a given height. At the same time, the continuum shape is independent of the emission angle, with only the normalization varying. We expect, however, that the

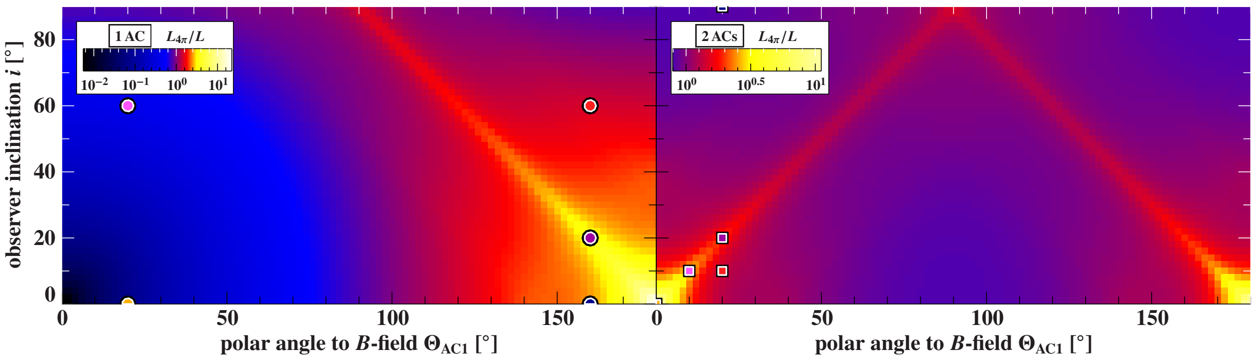

Fig. 7. Anisotropy of the flux-derived luminosity, $L_{4\pi}$ (Eq. 4), dependent on the geometry, i, and Θ_{AC} in units of the bolometric luminosity, L (Eq. 2). Left: Case of one accretion column. Right: Case of two antipodal accretion columns. The colored markers correspond to the geometrical cases of the observed spectra shown in Fig. 8 (left) and Fig. 9 (right), respectively.

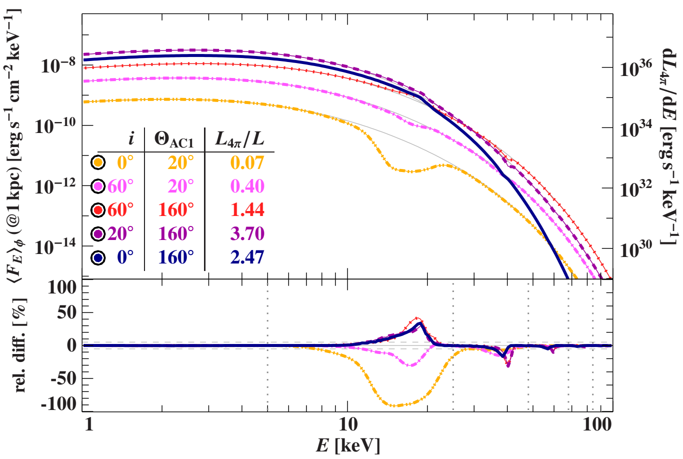

Fig. 8. Phase-averaged spectra of a single accretion column in the observer frame. Each spectrum corresponds to a different setup (i, Θ_{AC}) indicated in the table inlet. Solid gray lines correspond to the case without CRSFs. The bottom panel shows the relative difference of the spectra to their pure continuum contribution, where horizontal dashed gray lines mark ±5%. CRSFs energy ranges are indicated with the vertical dotted gray lines.

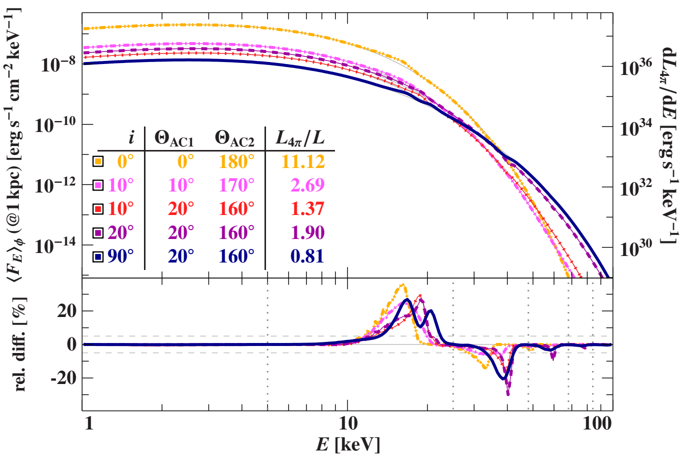

Fig. 9. Same as Fig. 8, but for two antipodal columns.

total flux in the rest frame of the neutron star is affected by mixed contributions of different plasma temperatures and boosting factors. In our model, the intrinsic height- and angle-integrated continuum of individual columns is well described by $\Gamma^\star = 0.23$ and $E^\star{}_{\text{fold}} = 5.2\,\text{keV}$. As expected, the folding energy roughly corresponds to the plasma temperature at the height of peak emission (Fig. 1; Paper I, Fig. 5). The plasma temperature increases from 0.6 keV at a height of 5 km to 9.2 keV at the base of the column and decreases toward the column walls relative to the center (Paper I, Fig. 3).

For different geometries, the observed spectra include contributions only from the visible parts of the column at various heights. Height-dependent light bending, gravitational redshift, and shadowing can significantly alter the continuum spectra compared to those integrated in the column rest frame. Across different geometries, $\overline{\Gamma}$ ranges from 0.09 to 0.34 for the one-column case, and from 0.09 to 0.27 for two columns. In both cases, $\overline{\Gamma}$ decreases as the geometry approaches $i + \Theta_{AC1,2} = 180°$. The mean folding energy, $\overline{E}_{\text{fold}}$, initially increases as $i + \Theta_{AC1,2}$ approaches 180°. It then decreases once the geometry places the hotter bottom parts of the column within the shadow region for a significant fraction of the neutron star's rotational phase. In both the single-column and antipodal two-column cases, $\overline{E}_{\text{fold}}$ ranges from 2.8 keV to 3.6 keV. We note that the values of $\overline{E}_{\text{fold}}$ are significantly lower than the intrinsic folding energy, $E^\star{}_{\text{fold}}$, due to gravitational redshift (Paper I, Eq. A.24).

3.4.2. Fundamental CRSF

As expected, the observed cyclotron lines also strongly depend on the geometry as it directly influences the visible emission angles (Figs. 8, 9). In comparison to the cyclotron lines in the rest frame of the column (see Paper I, Fig. 6), the lines are redshifted to lower energies, while the variation in the line energy seems to have decreased. The observed CRSF energy is related to the intrinsic CRSF energy (Paper I, Eq. 7) by

$$E_{\text{CRSF}n} = E'_{\text{CRSF}n} \frac{\sqrt{1-\beta^2}}{1+\beta\mu^\star} \sqrt{1 - \frac{R_s}{R}}, \tag{12}$$

where n is the number of the cyclotron harmonic and $\beta = v_0/c$ is a bulk velocity expressed in the speed of light, c. The large range of $E^\star_{\text{CRSF}}$ in the rest frame of the neutron star is caused by the boosting due to the bulk velocity. The observer, however, sees directly only photons emitted up to a maximum emission angle $\eta^\star$ (Eq. 1), which decreases the variation in E_{CRSF}. As before (Paper I), the appearance of the fundamental cyclotron line in emission is generally caused by strong emission wings which are formed around the line core due to redistribution effects (Schwarm et al. 2017a; Schönherr et al. 2007).

The large variety of shapes of the fundamental CRSF prevents one from comparing it with a simple absorption line model. To investigate the dependency of fundamental CRSF on the geometry, we therefore used the 5–25 keV equivalent width,

$$W = \int_{E_{\mathrm{lo}}}^{E_{\mathrm{hi}}} \frac{F_E - \mathcal{F}_E}{\mathcal{F}_E} \mathrm{d}E \quad \text{and} \quad \overline{W} = \int_{E_{\mathrm{lo}}}^{E_{\mathrm{hi}}} \frac{\langle F_E \rangle_\phi - \langle \mathcal{F}_E \rangle_\phi}{\langle \mathcal{F}_E \rangle_\phi} \mathrm{d}E\,, \tag{13}$$

where $\mathcal{F}_E$ is the observed flux without CRSFs; that is, using $\mathcal{I}_E$ (Paper I, Eq. 1) instead of I_E (Paper I, Eq. 5). For a single accretion column, we see the CRSF in absorption for geometries with $\Theta_{\mathrm{AC}} \approx i$, where certain phases allow the accretion column to be observed from above, at relatively small angles to the magnetic field ($\lesssim 45°$; see Paper I, Fig. 6). The minimum and maximum equivalent width are -10.4 keV and 2.4 keV, respectively.

To get a better understanding of this behavior, we can look again at Fig. 1, which shows the strength of the fundamental CRSF with respect to the continuum in the rest frame of the emitter. We define this line strength as

$$S' = 2\pi r_{\mathrm{AC}} \int_{E'_{\mathrm{lo}}}^{E'_{\mathrm{hi}}} \int_{-\pi/2}^{\pi/2} I'_{E'} - \mathcal{I}'_{E'} \mathrm{d}\eta_{\mathrm{S}} \mathrm{d}E'. \tag{14}$$

Besides the decrease in the line strength with height due to the decrease in the overall emissivity, we see that for $45° < \eta' < 135°$ the fundamental CRSF is in emission. It is in absorption only for $\eta' > 135°$ and $\eta' < 45°$; that is, for small angles with respect to the magnetic field.

Although the absolute value of the line strength is greater in absorption than in emission, several conditions cause the observed fundamental line to appear most prominently in emission. First, the specific intensity of the column follows a fan beam pattern proportional to $\sin\eta'$ (Paper I, Eq. 1), with peak emissivity perpendicular to the magnetic field, $\eta' = 0°$. Second, the solid angle over which the line is visible in emission is much larger than for the absorption. Finally, the light bending further enhances the observed flux for those angles where the line is in emission.

In the antipodal two-column case (Fig. 9) and the asymmetric configuration, the fundamental CRSF appears in emission for all geometries. This behavior – which contradicts observations – arises because of the contribution from the front column, which exhibits the absorption line, is outshined by the back column. The back column is seen under larger angles with respect to the B field, where the fundamental CRSF is mainly in emission due to the strong emission wings (see Paper I, Fig. 6). As a result, the equivalent width in the two-column case lies in a much smaller range, between 1.1 and 1.7 keV.

3.4.3. Second and higher harmonics

Contrary to the fundamental CRSF, its higher harmonics are always observed in absorption. Their shape is clearly asymmetric and has a shallow extended lower energy flank. Nevertheless, the higher harmonics are well approximated by a Gaussian absorption line. We parameterize the shape of the harmonic CRSFs using the `gabs` model, which describes an absorption line with a Gaussian optical depth profile. In the single column case the line energy of the second harmonic varies between 25 keV and 40 keV. Adding the second antipodal column increases the minimum line energy to 32 keV in the phase-averaged spectra.

Table 1. Ranges and phase amplitudes of the observed quantities.

Parameter	Single column $\overline{\min}$	Single column $\overline{\max}$	Single column A	Antipodal columns $\overline{\min}$	Antipodal columns $\overline{\max}$	Antipodal columns A
$L_{4\pi}/L$	10^{-3}	22	...	0.8	11	...
δF	0.00	1.00	1.00	0.00	0.87	0.87
Γ	0.09	0.34	0.24	0.09	0.27	0.17
E_{fold} [keV]	2.8	3.6	0.81	2.8	3.6	0.81
W_{CRSF1} [keV]	-10.4	2.4	12.8	1.1	1.7	0.6
W_{CRSF2} [keV]	-1.5	-0.5	1.0	-1.5	-0.6	0.9
E_{CRSF2} [keV]	25	40	15	32	40	9
σ_{CRSF2} [keV]	0.9	10.0	9.1	0.9	4.9	3.2
d_{CRSF2} [keV]	0.4	2.6	2.2	0.4	1.6	1.1
τ_{CRSF2}	0.06	0.48	0.42	0.06	0.45	0.39

Notes. Columns show the minimum, $\overline{\min}$, and maximum, $\overline{\max}$, values in the phase-averaged spectra and the maximum phase amplitudes, A, in the phase-resolved spectra for a single and two antipodal columns, respectively.

Across different geometrical configurations the width of the harmonic is anticorrelated to its energy. This anticorrelation is due to angle-dependent boosting factor in Eq. (12) and the dependence of the width of the cyclotron resonance on the angle to the magnetic field (e.g., Schwarm et al. 2017b)[2]. The appearance of the line varies from narrow to very broad as a function of geometry in a range of 0.9–10.0 keV in the one-column case, while in the two-column case the width varies less, between 0.9 and 4.9 keV. While the one- and two-column cases show a very different behavior for the line energy and width, the optical depth of the harmonic is largely independent of the number of accretion columns. In both cases considered here the optical depth is in a similar range of 0.06–0.48. Furthermore, there is a clear anticorrelation between the width and optical depth of the CRSF, which can be derived from the theoretical cyclotron scattering cross sections (e.g., Schwarm et al. 2017a,b). In particular, the lines are predicted to be wide and shallow for small viewing angles with respect to the B field, while they are narrow and deep for viewing angles approximately perpendicular to the B field. We note that this anticorrelation is preserved in the transformation from this intrinsic frame.

Although we are not able to parameterize the fundamental CRSF, its line energy varies approximately with the same factor as for the second harmonic. For our model, $\overline{E}_{\mathrm{CRSF2}}/E'_{\mathrm{CRSF2}} = 0.43$–$0.70$ for the single column and 0.55–0.70 for the antipodal columns, where $E'_{\mathrm{CRSF2}} = 58$ keV (Paper I, Eq. 7). The higher cyclotron harmonics, $n > 2$, behave in a similar way as the second harmonic, however, the line strength reduces with increasing harmonic number n (Figs. 8 and 9).

3.4.4. Phase and geometry variability

Table 1 shows an overview of the previously discussed observables, their minimum and maximum values occurring in the phase-averaged spectra. In addition, we show there the maximum phase amplitude in the phase-resolved spectra, A. Phase amplitude denotes the difference between the maximum and minimum value as function of pulse phase for a given parame-

[2] Note that geometries for which parts of the column are in the shadow region the line energy might still change even without bulk velocity due to the B field gradient. In that case, however, the corresponding geometry dependence would look different.

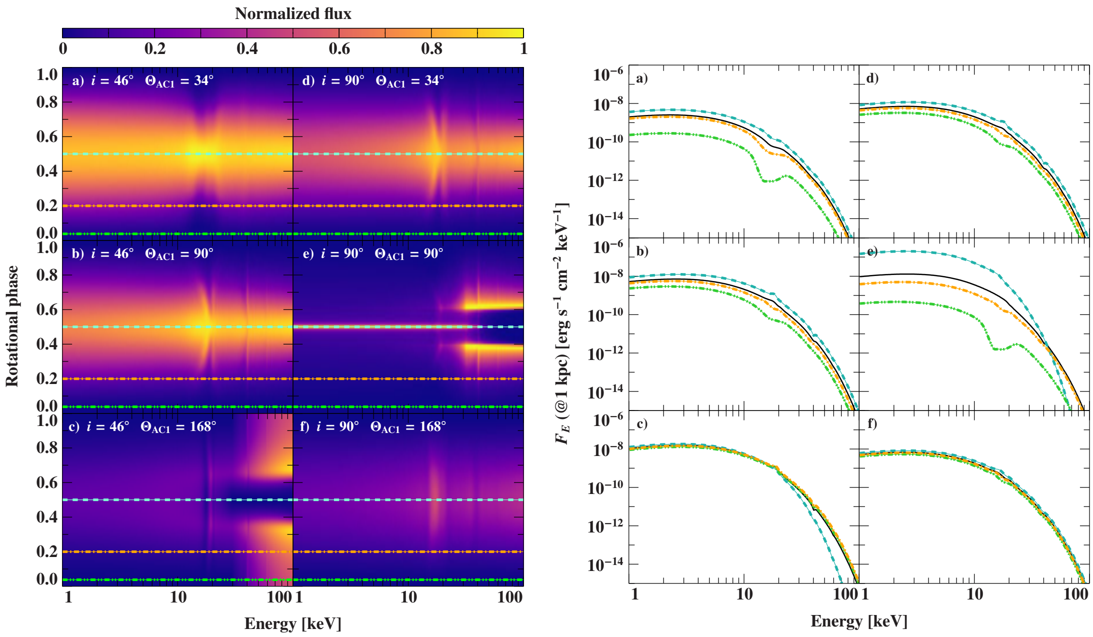

Fig. 10. Phase-energy flux variability. Left: Normalized observed phase and energy-dependent flux, $\tilde{F}_E(\phi) = (F_E(\phi) - \min(F_E)_\phi)/(\max(F_E)_\phi + \min(F_E)_\phi)$, for different single column geometries (i, Θ_{AC1}). The maximum value within each energy bin corresponds to the pulsed fraction. Right: Spectra for selected rotational phases, indicated in the left panel by the same line styles.

ter and geometry. The maximum phase amplitude then gives the maximum of these phase amplitudes occurring for all geometries[3]. For the two-column setup, the highest values of the phase amplitude; that is, the strongest phase variability, occurs for geometries with $\Theta_{AC1} \approx i$ and $i \gtrsim 20°$ for all spectral parameters discussed above. The lowest variability appears at low values of either i or $\Theta_{AC1/2}$, $\lesssim 10°$.

It is noticeable that the range in which the phase-averaged values vary is equal to the maximum phase amplitude (i.e., columns of Table 1 show $\overline{\max} - \overline{\min} \approx A$). This observation is easily explained by the fact that we are looking at all possible combinations of i and Θ_{AC}. In particular, we see the minimum and maximum values in the phase-averaged spectra stepping through different polar angles Θ_{AC} for $i = 0°$, for which there are no pulsations ($\delta F = 0$). On the other hand, the maximum phase amplitude is related to the geometry for $i = \Theta_{AC} = 90°$. Both cases equally allow us to observe the magnetic field under all possible viewing angles.

Comparing the one-column with the antipodal two-column cases, the variability of the observables with geometry and phase are impacted in different ways. The second column significantly reduces the range and amplitude of the anisotropy factor, as well as the energy, and width of the harmonic CRSF. In contrast, other observables, such as the folding energy and the optical depth of the harmonic CRSF, remain largely unchanged between the one-column and the two-column cases.

3.5. Phase-energy maps

The variations in the energy- and phase-resolved flux, $F_E(\phi)$, with the geometry, (i, Θ_{AC}), are primarily influenced by the spectral shape of the continuum. Figure 10 displays phase-energy maps for several single-column geometric configurations and spectra for selected phases. The fluxes are normalized such that, within each energy bin, the maximum value corresponds to the pulse fraction: we subtract the minimum value in the bin and divide by $\max(F) + \min(F)$. For most geometries, the pulse profile is broad and single-peaked across the whole energy range (e.g., panels (a), (b), (d), and (f) in Fig. 10). The only noticeable deviations occur in a narrow band around the CRSF energies, most prominently near the fundamental cyclotron line, due to the dependence of the CRSFs on the viewing angle (Paper I, Fig. 6) For these geometries, phase-dependent spectral changes are also confined to the CRSF energies and the overall flux level.

A stronger energy dependence occurs for geometries that satisfy the condition given in Eq. (8), which in our setup corresponds to $140° \lesssim i+\Theta_{AC} \lesssim 220°$ (panels (c) and (f) in Fig. 10). In this case, the pulse profiles generally evolve from single-peaked at lower energies to double-peaked at higher energies. This variability is driven by the column passing through the shadow region and the region of strong light bending (see Fig. 2), in combination with the height- and energy-dependent properties of the emission profile. Specifically, the line of sight to the bottommost (and therefore hottest) part of the column is blocked at this phase (see Paper I, Figs. 3 and 5). Since the temperature determines the exponential cutoff (Paper I, Eq. 1) and thus the spectral hardness, this effect strongly influences the observed spectrum. As the column moves further into the shadow region, the observed spectrum softens because only the cooler, upper parts of the column become visible. At the same time, the observed luminosity increases due to strong light bending, which enhances the emission from these upper regions of the column. In this way, light bending compensates for the decrease in emissivity with height, leading to an overall increase in observed flux. The enhancement of the high-energy flux occurs before and after the passage through the shadow region, when the hot base of the column is directly visible and its emission is amplified by light bending.

[3] For example, the maximum phase amplitude of the photon index is given by $A_\Gamma = \max_{i,\Theta_{AC}} \left\{ \max_\phi \left[\Gamma\left(F_E(\phi)|_{i,\Theta_{AC}} \right) \right] - \min_\phi \left[\Gamma\left(F_E(\phi)|_{i,\Theta_{AC}} \right) \right] \right\}$, where $F_E(\phi)|_{i,\Theta_{AC}}$ is the energy- and phase-resolved flux observed for i and Θ_{AC}.

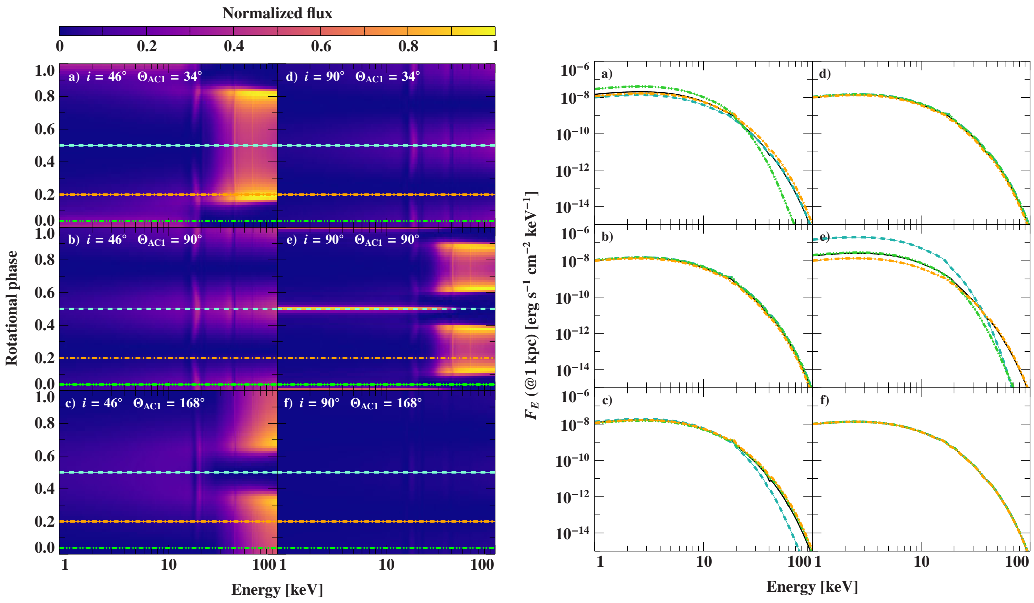

Fig. 11. Same as in Fig. 10, but for different antipodal column geometries (i, $\Theta_{AC1,2}$).

Figure 11 presents phase-energy maps for an antipodal two-column setup. They show same general behavior, but with more complexity due to the mixed contribution of the two columns. We would like to note that for geometries, where only the polar angles of the columns are swapped, (i, Θ_{AC2}, Θ_{AC1}), the phase-maps would appear identical to the case (i, Θ_{AC1}, Θ_{AC2}), with the only difference being a shift by half a rotational phase. This symmetry arises because the azimuthal positions of the columns remain unchanged.

The number of emission regions considered also plays an important role. Observables differ significantly between the single-column and two-column cases. Strong light bending boosts emission from the column on the far side of the neutron star, effectively outshining the front column. As a result, flux originating from small angles relative to the magnetic field becomes negligible in the total observed emission from both columns. This effect becomes more pronounced with increasing neutron star compactness and higher mass-accretion rates.

4. Discussion

4.1. Special geometries

We find that the observables depend strongly on the geometry, with configurations of particular interest corresponding to $i + \Theta_{AC1,2} \approx 180° \pm 40°$, where the range depends on the chosen column parameters and the neutron star compactness. In these cases, one of the columns aligns approximately with the observer's line of sight on the far side of the neutron star at a specific rotational phase (see Sect. 2.2). This alignment significantly enhances the visibility of the emitting region due to strong light-bending effects. The compactness of the neutron star determines the extent of the shadow region, which, combined with the vertical emissivity profile of the column, influences the strength of this effect on the observed flux.

The neutron star's compactness and the height dependence of the emission profile play a key role in shaping the observed flux. Within the framework of the Postnov et al. (2015) model, increasing the mass-accretion rate brightens the upper part of the accretion column (see their Fig. 3), which can enhance flux amplification due to strong light bending in special geometries where $i + \Theta_{AC1,2} \approx 180°$. This effect is pronounced when the emissivity extends above the maximum shadow height, $h_{\mathrm{S}}^{\max}$. Conversely, at lower mass-accretion rates, where emission is concentrated near the column base, and for higher compactness, the shadow region may fully obscure the emission, resulting in a pronounced dip in the pulse profile. A detailed quantitative analysis of compactness effects is beyond the scope of this work.

4.2. Phase dependence

Regarding the simulated pulse profiles, we find that narrow yet prominent peaks can be produced for geometries where $i + \Theta_{AC1,2} \approx 180°$ (see Fig. 3). Such sharp features are not expected for a fan-beam geometry, which typically emits into a wide solid angle. They arise due to strong light bending, when during a short phase interval, the projected area of the emitting region increases significantly, resulting in a short but intense pulse. The effect was previously found in works featuring similar columns, such as Meszaros & Riffert (1988), Nollert et al. (1989), Markozov & Mushtukov (2024). This effect, with a slightly larger offset between i and $\Theta_{AC1,2}$ and in combination with asymmetric column configurations, can produce peaks similar to those observed in, for example, KS 1947+300 (Fürst et al. 2014; Ballhausen et al. 2016; Epili et al. 2016) and IGR J16393−4643 (Islam et al. 2015; Bodaghee et al. 2016).

Another feature, apparent on phase-energy maps, is a transition from single-peak profiles at low energies to double-peak profiles at higher energies caused by obscuration of the hot base of the column. A similar transition has been observed, for example, in the phase–energy maps and pulse profiles of V 0332+53 during bright stages of its outbursts (Kreykenbohm et al. 2005; D'Aì et al. 2025). While shifts in these maps are often attributed to flux redistribution around CRSF energies (e.g., Ferrigno et al. 2011; Schönherr et al. 2014; Ferrigno et al. 2023), our results show that strong light bending and shadowing can also produce significant energy-dependent shifts in the pulse profile maxima, with a smoother behavior for asymmetrically located columns.

However, our model likely underestimates the impact of CRSFs on the phase shifts. In the current approach, reprocessing of the continuum radiation in the CRSF layer is based on precalculated tables: the angle-dependent CRSF shape is imprinted on the spectra, but no actual angle- and energy-redistribution occurs in this layer (see Sect. 2.2 in Paper I). As a result, the corresponding changes in the phase–energy maps are confined to the CRSF energies. A more detailed treatment of the redistribution would affect a broader range of energies in the vicinity of the resonance.

In addition, we note that we currently do not incorporate any reprocessing of the direct emission, which could occur due to interception by the accretion stream inside the magnetosphere or by matter above it (such as an accretion disk or the stellar wind of the companion). Such reprocessing is expected to affect the angular and spectral distribution of the soft X-ray emission.

4.3. Luminosity

The anisotropy factor, $L_{4\pi}/L$, arises mainly due to unknown luminosity distribution with observer inclination, magnetic pole positions, and emission patterns. This factor leads to systematic overestimation of L, especially for more compact neutron stars due to stronger light bending. Similar conclusions were reached by Markozov & Mushtukov (2024) for supercritical accretion with extended columns.

For our two-column setup, we find that the actual and isotropic, flux-derived luminosities can differ by up to a factor of 11. This discrepancy may be even larger if one considers the possibility of re-emission of flux intercepted by the neutron star atmosphere – an effect not included in our current model. The most extreme cases of flux amplification occur for specific viewing geometries; namely, when $i \approx \Theta_{\mathrm{AC1}}$ or $i \approx \pi - \Theta_{\mathrm{AC1}}$. For most other geometries, the effect is significantly weaker. A comparable geometry-dependent behavior was also reported by Markozov & Mushtukov (2024)[4]. However, the magnitude of the anisotropy factor also depends on the specific model setup and the underlying emission pattern, $\mathcal{I}'_{E'}$ (Paper I, Eq. 1).

Another source of uncertainty is the gravitational redshift. Its exact value depends not only on the neutron star's compactness but also on the spatial distribution of the emission. Based on theoretical predictions of mass–radius relations (see, e.g., Steiner et al. 2013; Annala et al. 2018), we find $R_{\mathrm{s}}/R_{\mathrm{NS}} \approx 0.15{-}0.74$. This range of compactness corresponds to gravitational redshifts of $z_{\mathrm{NS}} \approx 0.08{-}0.97$, yielding a gravitational correction factor of 0.26–0.85 for L and the intrinsic luminosity, $L^\star$ (Eq. 3). Combined, the anisotropy factor and the uncertainty in gravitational redshift can lead to an over- or underestimation of the intrinsic luminosity by up to a factor of ∼10.

Finally, a significant fraction of the fan-beam emission can be directed toward the neutron star surface and thus remain unobservable (see Sect. 2.1). In our model, 58% of the intrinsic luminosity from the column is intercepted by the star. This fraction increases with higher bulk velocities, due to stronger downward beaming, and with accretion rate, as the column height grows (Postnov et al. 2015). Therefore, reflection or reprocessing by the neutron star surface must be considered when relating L to the intrinsic luminosity. A similar effect was described by Poutanen et al. (2013), who found even higher captured fractions due to a different emission profile. The role of beaming and captured emission has also been discussed by Kylafis et al. (2021). Importantly, emission beaming by the accretion flow should be computed self-consistently, accounting for the coupling between the column's hydrodynamics and angle- and energy-dependent radiative transfer – an aspect not included in our current model. As noted in Paper I, the overall boosting may also be overestimated. Most models of this class obtain the reflection component by assuming isotropic reemission from the neutron star surface (Nollert et al. 1989; Kraus et al. 2003; Markozov & Mushtukov 2024). Such a simplified treatment is often adopted because of the overall complexity of the problem. A more realistic description of the reprocessing, however, must account for anisotropy introduced by the strong magnetic field and resonant Comptonization (see, e.g., Meszaros & Nagel 1985a,b).

4.4. Continuum

The photon index and folding energy show a clear dependence on geometry, which results from the integrated emission from regions with varying plasma temperatures, corresponding to different column heights, as well as from changes in viewing angle. The intrinsic continua calculated by Postnov et al. (2015), for mass-accretion rates within an order of magnitude, differ primarily in flux level. We therefore expect that an increased mass-accretion rate would mainly result in harder spectra during the column's passage through the shadow region, due to an overall temperature increase in the upper parts of the column. Following Postnov et al. (2015), the temperature profile used here assumes thermodynamic equilibrium, which breaks down in the outer column layers above the accretion mound. A more accurate treatment could yield different results. For example, Gornostaev (2021) and Gornostaev (2025) obtain an inverted temperature profile compared to ours, which would affect both the continuum shape and CRSF width. Finally, we considered only the directly observable emission. Emission reflected from the neutron star atmosphere can alter the observed spectral hardness (Postnov et al. 2015).

Observations of accreting X-ray pulsars show a broad range of phase-averaged spectral shapes, characterized by varying photon indices and folding energies. For the majority of sources, the photon index derived from the phase-averaged spectra leis in the range $\overline{\Gamma} \approx 0{-}2.2$ and $\overline{E}_{\mathrm{fold}}$ ranges from 2 keV to 49 keV (see, e.g., Table 1.9 in Falkner 2018)[5]. While our simulated values (Table 1) fall within these ranges, they tend to be lower than those observed in most sources.

The observed variability of the continuum with pulse phase covers a wide range with maximum amplitudes between $A_\Gamma = 0.0{-}1.8$ and $A_{E_{\mathrm{fold}}} = 0.3{-}38$ keV (e.g., Makishima et al. 1999; Fürst et al. 2011; Maitra et al. 2012; Hemphill et al. 2016; Ferrigno et al. 2016). In comparison, the maximum phase variability of the continuum in our simulations is rather small ($A_\Gamma \leq 0.17$, $A_{E_{\mathrm{fold}}} \leq 0.81$ keV; Table 1).

The continuum considered here assumes all photons are emitted in the extraordinary polarization mode (see, e.g., Mészáros & Ventura 1978; Pavlov et al. 1980, for the definitions of polarization modes). Radiative transfer simulations that include polarization effects, accounting for both magne-

[4] We note that our flux-derived isotropic luminosity corresponds to "apparent" luminosity in Markozov & Mushtukov (2024). However, the definition of their "actual" luminosity is not fully clear, as it is described both as the flux integrated in the neutron star rest frame and as averaged over all observers (see their Eq. 10 and the related discussion). In our definitions, the first case corresponds to the intrinsic luminosity, $L^\star$, while the second corresponds to the quantity given by our Eq. 2. We interpret the expression given in Eq. 10 of Markozov & Mushtukov (2024) as equivalent to our $L_{4\pi}/L$.

[5] Note that these values were obtained based on different continuum models, e.g., `CutoffPL`, `HighEcut`.

tized plasma and vacuum birefringence, and couple the continuum with cyclotron resonance treatment reveal more complex continuum shapes and beam patterns (Soffel et al. 1985; Sokolova-Lapa 2023).

4.5. CRSF

Our simulations show that for any two-column geometry in this setup, the fundamental CRSF appears in emission with equivalent widths large enough to be detectable. The reasons for this effect are discussed in Sect. 3.4.2. Asymmetrically positioned columns do not significantly alter this result. Among all known accreting X-ray pulsars exhibiting CRSFs, there is no evidence of a CRSF in emission. Theoretical models predict strong emission wings for the fundamental line due to photon spawning or redistribution within the cyclotron resonance (see Isenberg et al. 1998; Nishimura 2008; Schwarm et al. 2017a,b; Kumar et al. 2022, and references therein). However, the visibility of these emission features clearly depends on the continuum shape, becoming more pronounced for harder spectra (Kumar et al. 2022). We also expect this effect to weaken at higher magnetic field strengths.

The fundamental CRSF is observed in absorption at small angles to the magnetic field and in emission at roughly perpendicular angles. One possible solution is a significant contribution from emission at the top of the column, where radiation might escape through optically thin regions known as photon bubbles (Klein & Arons 1989). Alternatively, the direct fan-beam emission from the column could be outshone by reflection off the neutron star surface. Kylafis et al. (2021) demonstrated that reflected spectra can produce a CRSF with centroid energy near the cyclotron energy at the magnetic pole, though the feature tends to be shallower than usually observed[6]. It remains unclear whether prominent emission features caused by higher-order cyclotron processes can be suppressed in such scenarios. However, detailed simulations indicate that slab-like geometries can indeed produce purely absorption features (e.g., Schwarm et al. 2017b).

Another factor that could partially improve the situation is a neutron star with lower compactness, resulting in a larger shadow region (Fig. 2). Combined with an emissivity distribution confined to a small height range, lower compactness reduces the effect of strong light bending. As a result, emission from the front column, seen at small angles to the magnetic field and responsible for a deep fundamental CRSF in absorption, would be visible even in two-column configurations. However, it is only the case for some geometries and limited pulse phases.

We note that a likely reason for the dramatic extent of the emission line problem is the low optical depth chosen for CRSF formation in our model (see Paper I). Detailed cyclotron line simulations clearly demonstrate that the optical depth of the line-forming region moderates the shape of the fundamental CRSF and the strength of the emission wings. Ideally, the optical depth should extend to a level beyond which increasing it further no longer impacts line formation. However, such high depths are not included in the current precomputed CRSF tables. While we plan to address this limitation in future work, it is unclear whether this will fully resolve the issue of strong emission wings. A more comprehensive treatment would be computationally expensive and lies beyond the scope of this study.

Besides the fundamental CRSF, we also find that the first three harmonics ($n = 2, 3, 4$) in our simulated spectra behave similarly, though with rapidly decreasing equivalent widths at higher harmonic orders (Table 1). A detailed investigation of the second harmonic shows a strong anticorrelation between the line width and optical depth. The second and higher harmonics also exhibit a clear asymmetry, with shallow, extended low-energy flanks. Similar asymmetries have been reported in a few observational studies (see, e.g., Pottschmidt et al. 2005; Fürst et al. 2015).

Accounting for the relativistic bulk velocity of the in-falling plasma is important, as the resulting angle-dependent boosting (Paper I, Eq. 10) can cause significant phase-dependent variations in the CRSF energy. While the intrinsic line energy is nearly independent of the viewing angle (Paper I, Eq.7), the inclusion of the bulk velocity introduces a strong angular dependence, leading to observable phase variability (Eq. 12). Many existing interpretations of CRSF energy variability with phase rely on the changing visibility of regions with different magnetic field strengths. However, our simulations show that even in an antipodal two-column setup, the phase-resolved CRSF energy can vary by up to 23% around its phase-averaged value purely due to angle-dependent boosting.

5. Conclusions

In this study, we analyzed various observables using an accretion column model with a fixed mass-accretion rate and surface magnetic field strength, exploring a range of possible geometric configurations. The observables were derived using a model for the internal emission from the radiation-dominated accretion column, which incorporates physically motivated continua and CRSF formation, and accounts for the column structure and relativistic bulk velocities near the column walls. We find similar features for pulse profiles as in Nollert et al. (1989), whose column model features similar physical components. We extended the study to other observables, such as pulse fraction, luminosity, spectra, and phase–energy maps, and systematically explored a broad range of geometries. We find that the general behavior of the directly observed flux reproduces results from earlier models that either simplified the spectral treatment (Kraus et al. 2003) or neglected energy dependence (Markozov & Mushtukov 2024), while still incorporating key effects such as fan-beam-like emission (typically not energy-dependent), down-boosting by bulk flow, height-dependent emissivity, and light bending. Our simulations recover features such as strong surface illumination, flux amplification, and characteristic trends in pulse profiles for specific geometries. In addition, we performed a detailed study of phase-averaged and phase-resolved spectra with CRSFs, which has not been previously addressed. Although our study is similar to Nollert et al. (1989), based on a fixed internal emission model, we discuss some expected influence on the observables from variations in key physical parameters, such as mass-accretion rate, magnetic field strength, and the initial bulk-flow velocity (see Sect. 4).

The variability of the observables across the geometry space is largely driven by special geometries, when one of the columns is on the dark side of the neutron star and roughly aligned with the line of sight during rotation. During these phases, strong light bending amplifies emission from the upper part of the column, while the lower part is eclipsed by the shadow region. This produces a pronounced flux peak in the pulse profile at soft X-ray energies and a dip at higher energies. The variation in this effect across a range of geometries gives rise to a variety of

[6] They also found, however, that within the frame of their model they do not reproduce the observed negative correlation between CRSF energy and luminosity.

phase–energy maps, suggesting that geometrical effects may be an important driver of the diversity observed in phase–energy maps.

Due to the height-dependent emission in our model, the observed spectra, originating from the cooler upper region of the column, are softer. This holds both for phases corresponding to the shadow passage and for phase-averaged spectra of the special geometries compared to other ones. For lower emission scale heights, as expected at lower mass-accretion rates, the effect may instead produce pronounced dips. Whether the spectrum appears softer or harder depends on the temperature distribution. These special geometries also show the largest phase variability in spectral parameters. However, even for these geometries, the overall phase variability remains well below that sometimes observed in accreting X-ray pulsars, which might indicate a more complex energy-dependent beaming pattern than assumed in this work.

We also note that the flux-derived luminosity is subject to systematic errors due to the anisotropy of neutron star emission, which is further enhanced by light-bending effects. Combined with uncertainties in the gravitational redshift, these corrections are on the order of 10.

The most contradictory result is the one that we obtain for the fundamental line. In the phase-averaged spectra for any two-column configuration, the predicted fundamental CRSF is solely observed in emission. The emission feature arises from the strong emission wings observed under large angles to the magnetic field, which dominate the directly observable emission in the model[7]. We discuss possible reasons for this problem, which are likely at least partly related to the treatment of the CRSF-forming layer in our model. We also note that a pencil-beam-like emission component, either from the reflection halo or the direct emission from the column close to the magnetic field lines, would result in an absorption line profile. Considering the strong illumination of the neutron star surface in our model, investigating the reflection component is one of the important following steps.

In this work, we emphasize that a thorough exploration of the parameter space of a complex theoretical model is a mandatory preliminary step before any meaningful comparison with observations, such as spectral fitting of observational data. We identify geometric effects as one of the key factors influencing the observables and stress that the phase- and geometry-dependent contributions of emission regions with different plasma states, further modified by gravitational effects, can significantly deviate the observed spectral parameters from those of the intrinsic column emission. This fact should not be overlooked when attempting to infer physical conditions inside the accretion column, such as plasma temperature and magnetic field strength, from observed spectra.

Acknowledgements. We dedicate this work to the memory of our beloved colleagues, Dr. Katja Pottschmidt and Dr. Maurizio Falanga, who unexpectedly passed away last year. They provided invaluable contributions to this study and their work continues to be an integral part of this paper. We thank the anonymous referee for their constructive comments, which helped improve the clarity and quality of this manuscript. This work has been funded by the Deutsche Forschungsgemeinschaft under the DFG grant number WI 1820-10/1. The work of KP is supported by RFBR grant 18-502-12025. The work of ESL is also supported by the FAU Emerging Talents Initiative. The material is based upon work supported by NASA under award number 80GSFC21M0002. Astrophysics research at the Naval Research Laboratory is supported by the NASA Astrophysics Explorer Program. The authors are grateful to M. Gornostaev, M. Sasaki, and J. J. R. Stierhof for valuable comments and discussions. The fruitful discussions within the XMAG (former MAGNET) collaboration also had a very positive impact on this work. We acknowledge the support from the Faculty of the European Space Astronomy Centre (ESAC). This research has made use of ISIS functions (ISISscripts) provided by ECAP/Remeis observatory and MIT (`http://www.sternwarte.uni-erlangen.de/isis/`). The figures in this work have been produced with the `S-Lang` module `slxfig` developed by J. Davis.

[7] To date, no cyclotron lines in emission have been reported in the spectra of accreting X-ray pulsars, although recent analysis suggests the presence of emission wings in the spectrum of V 0332+53 (the wings are, however, much weaker than in our model; D'Aì et al. 2025).

References

Annala, E., Gorda, T., Kurkela, A., & Vuorinen, A. 2018, Phys. Rev. Lett., 120, 172703
Ballhausen, R., Kühnel, M., Pottschmidt, K., et al. 2016, A&A, 591, A65
Bodaghee, A., Tomsick, J. A., Fornasini, F. M., et al. 2016, ApJ, 823, 146
D'Aì, A., Maniadakis, D. K., Ferrigno, C., et al. 2025, A&A, 694, A316
Einstein, A. 1936, Science, 84, 506
Epili, P., Naik, S., & Jaisawal, G. K. 2016, Res. Astron. Astrophys., 16, 77
Falkner, S. 2018, Dissertation, Friedrich-Alexander-Universität Erlangen-Nürnberg, Germany
Falkner, S., Sokolova-Lapa,, E., Schwarm, F. W., et al. 2026, A&A, 711, A224
Ferrigno, C., Falanga, M., Bozzo, E., et al. 2011, A&A, 532, A76
Ferrigno, C., Pjanka, P., Bozzo, E., et al. 2016, A&A, 593, A105
Ferrigno, C., D'Aì, A., & Ambrosi, E. 2023, A&A, 677, A103
Fürst, F., Kreykenbohm, I., Suchy, S., et al. 2011, A&A, 525, A73
Fürst, F., Pottschmidt, K., Wilms, J., et al. 2014, ApJ, 784, L40
Fürst, F., Pottschmidt, K., Miyasaka, H., et al. 2015, ApJ, 806, L24
Gornostaev, M. I. 2021, MNRAS, 501, 564
Gornostaev, M. I. 2025, MNRAS, 544, 3229
Hemphill, P. B., Rothschild, R. E., Fürst, F., et al. 2016, MNRAS, 458, 2745
Isenberg, M., Lamb, D. Q., & Wang, J. C. L. 1998, ApJ, 505, 688
Islam, N., Maitra, C., Pradhan, P., & Paul, B. 2015, MNRAS, 446, 4148
Klein, R. I., & Arons, J. 1989, in Two Topics in X-Ray Astronomy, Volume 1: X Ray Binaries. Volume 2: AGN and the X Ray Background, 1, 89
Kraus, U., Rebetzky, A., Herold, H., et al. 1989, ESA Special Publ., 296, 433
Kraus, U., Zahn, C., Weth, C., & Ruder, H. 2003, ApJ, 590, 424
Kreykenbohm, I., Mowlavi, N., Produit, N., et al. 2005, A&A, 433, L45
Kumar, S., Bala, S., & Bhattacharya, D. 2022, MNRAS, 515, 914
Kylafis, N. D., Trümper, J. E., & Loudas, N. A. 2021, A&A, 655, A39
Laycock, S. G. T., Cappallo, R. C., Pradhan, P., Christodoulou, D. M., & Paul, B. 2025, ApJ, 978, 80
Loudas, N., Kylafis, N. D., & Trümper, J. 2024, A&A, 685, A95
Maitra, C., Paul, B., & Naik, S. 2012, MNRAS, 420, 2307
Makishima, K., Mihara, T., Nagase, F., & Tanaka, Y. 1999, ApJ, 525, 978
Markozov, I. D., & Mushtukov, A. A. 2024, MNRAS, 527, 5374
Meszaros, P., & Nagel, W. 1985a, ApJ, 298, 147
Meszaros, P., & Nagel, W. 1985b, ApJ, 299, 138
Meszaros, P., & Riffert, H. 1988, ApJ, 327, 712
Mészáros, P., & Ventura, J. 1978, Phys. Rev. Lett.,, 41
Mushtukov, A. A., Verhagen, P. A., Tsygankov, S. S., et al. 2018, MNRAS, 474, 5425
Mushtukov, A. A., Suleimanov, V. F., Tsygankov, S. S., & Portegies Zwart, S. 2021, MNRAS, 503, 5193
Nishimura, O. 2008, ApJ, 672, 1127
Nollert, H. P., Ruder, H., Herold, H., & Kraus, U. 1989, A&A, 208, 153
Pavlov, G. G., Shibanov, I. A., & Iakovlev, D. G. 1980, Ap&SS, 73, 33
Pechenick, K. R., Ftaclas, C., & Cohen, J. M. 1983, ApJ, 274, 846
Postnov, K. A., Gornostaev, M. I., Klochkov, D., et al. 2015, MNRAS, 452, 1601
Pottschmidt, K., Kreykenbohm, I., Wilms, J., et al. 2005, ApJ, 634, L97
Poutanen, J., Mushtukov, A. A., Suleimanov, V. F., et al. 2013, ApJ, 777, 115
Rebetzky, A., Herold, H., Maile, T., Ruder, H., & Wolf, K. 1988, A&A, 205, 215
Rebetzky, A., Bock, U., Herold, H., Kraus, U., & Maile, T. 1989, A&A, 225, 137
Schönherr, G., Wilms, J., Kretschmar, P., et al. 2007, A&A, 472, 353
Schönherr, G., Schwarm, F.-W., Falkner, S., et al. 2014, A&A, 564, L8
Schwarm, F.-W., Ballhausen, R., Falkner, S., et al. 2017a, A&A, 601, A99
Schwarm, F.-W., Schönherr, G., Falkner, S., et al. 2017b, A&A, 597, A3
Soffel, M., Herold, H., Ruder, H., & Ventura, J. 1985, A&A, 144, 485
Sokolova-Lapa, E. 2023, Dissertation, Friedrich-Alexander-Universität Erlangen-Nürnberg, Germany
Sokolova-Lapa, E., Gornostaev, M., Wilms, J., et al. 2021, A&A, 651, A12
Steiner, A. W., Lattimer, J. M., & Brown, E. F. 2013, ApJ, 765, L5
Thorne, K. S. 1977, ApJ, 212, 825
West, B. F., Wolfram, K. D., & Becker, P. A. 2017, ApJ, 835, 130
Wolff, M. T., Becker, P. A., Gottlieb, A. M., et al. 2016, ApJ, 831, 194

Appendix A: Asymmetric column setup

For completeness, we also show some selected results for an asymmetric two-column configuration based on the setup of Ferrigno et al. (2011). The relative displacements between the columns are fixed to $\Delta\Phi_{\mathrm{AC}} = \Phi_{\mathrm{AC1}} - \Phi_{\mathrm{AC2}} - \pi = -65°$ and $\Delta\Theta_{\mathrm{AC}} = \pi - \Theta_{\mathrm{AC1}} - \Theta_{\mathrm{AC2}} = -42°$. While these relative offsets are kept fixed, we vary Φ_{AC1} and Φ_{AC2}, and explore the dependence on i and Θ_{AC} for both the one-column and antipodal two-column setups.

The overall behavior of the asymmetric two-column setup is similar to the antipodal configuration, with the modification of the phase dependence determined by the imposed displacement $\Delta\Theta_{\mathrm{AC}}$. In particular, the dependence of the pulsed fraction and luminosity on geometry exhibits a corresponding shift of the pattern (see Figs. A.2 and A.1).

Phase–energy maps for asymmetric configurations exhibit a significant variety of shapes, while their evolution with energy can appear smoother. Overall, the asymmetry introduces additional diversity in the observables without qualitatively altering the general trends seen in the symmetric case. Figure A.4 shows examples of phase-energy maps and spectra at selected phases.

While asymmetry alters the phase behavior of the observed flux (see Sect. 3.5), the ranges and amplitudes of the parameters are only slightly different compared to the symmetric antipodal case. The main exception is the equivalent width of the fundamental CRSF, which has a higher range, 0.7–2.4 and amplitude, $A = 4.7$ keV, for the asymmetric columns.

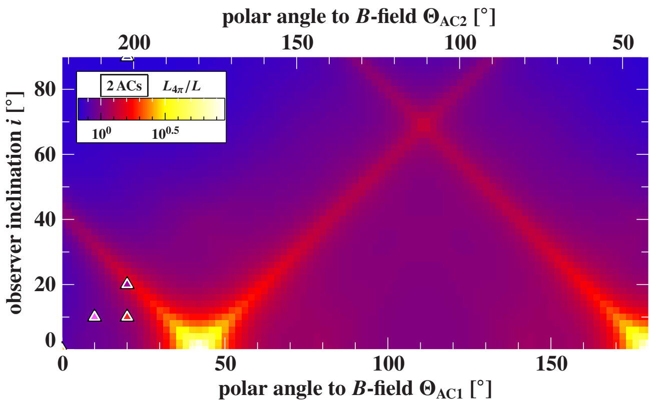

Fig. A.1. Anisotropy of the flux-derived luminosity for the asymmetric setup.

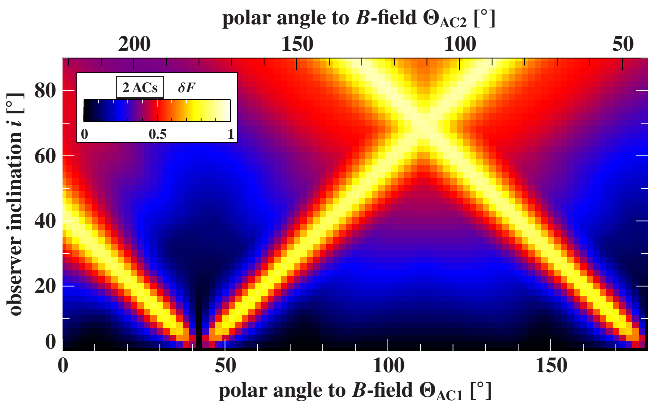

Fig. A.2. Pulsed fraction of energy-integrated pulse profiles for the asymmetric setup.

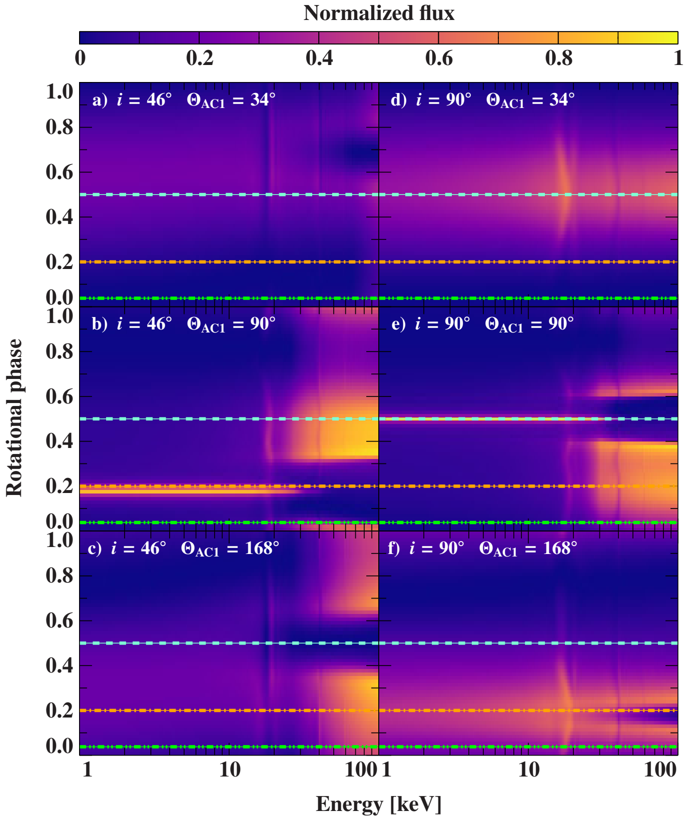

Fig. A.3. Normalized observed phase and energy-dependent flux for the asymmetric setup, $\tilde{F}_E(\phi) = (F_E(\phi) - \min(F_E)_\phi)/(\max(F_E)_\phi + \min(F_E)_\phi)$, for different geometries (i, Θ_{AC1}). The maximum value within each energy bin corresponds to the pulsed fraction value.

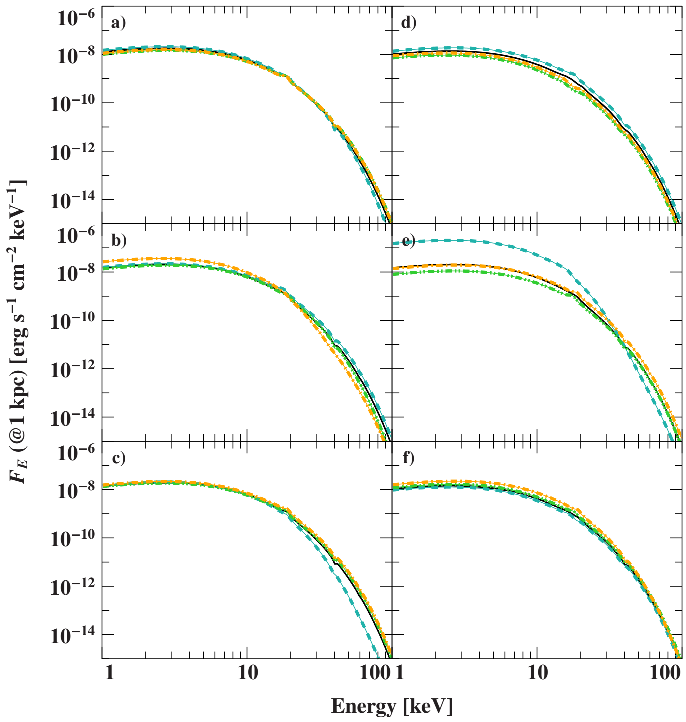

Fig. A.4. Spectra for selected rotational phases and geometries, as indicated in Fig. A.4.